

Electronic Supplementary Information: Run-and-tumble dynamics of active giant vesicles

Vivien Willems^a, Alexandre Baron^{a,b}, Daniel Fernandez-Matoz^c,
Gianna Wolfisberg^d, Jean-Christophe Baret^{a,b}, Eric Dufresne^e, and Laura Alvarez^{a*}

^aUniv. Bordeaux, CNRS, CRPP, UMR 5031, F-33600 Pessac, France

^bInstitut Universitaire de France, 1 rue Descartes, 75231 Paris Cedex 05, France

^cDepartment of Theoretical Physics, Complutense University of Madrid, Madrid, 28040, Spain

^dLaboratory for Soft Living Materials, Department of Materials, ETH Zurich, Zurich, Switzerland

^eDepartment of Materials Science and Engineering, Cornell University, Ithaca, NY, 14853, USA.

*To whom correspondence should be addressed;

E-mail: laura.alvarez-frances@u-bordeaux.fr

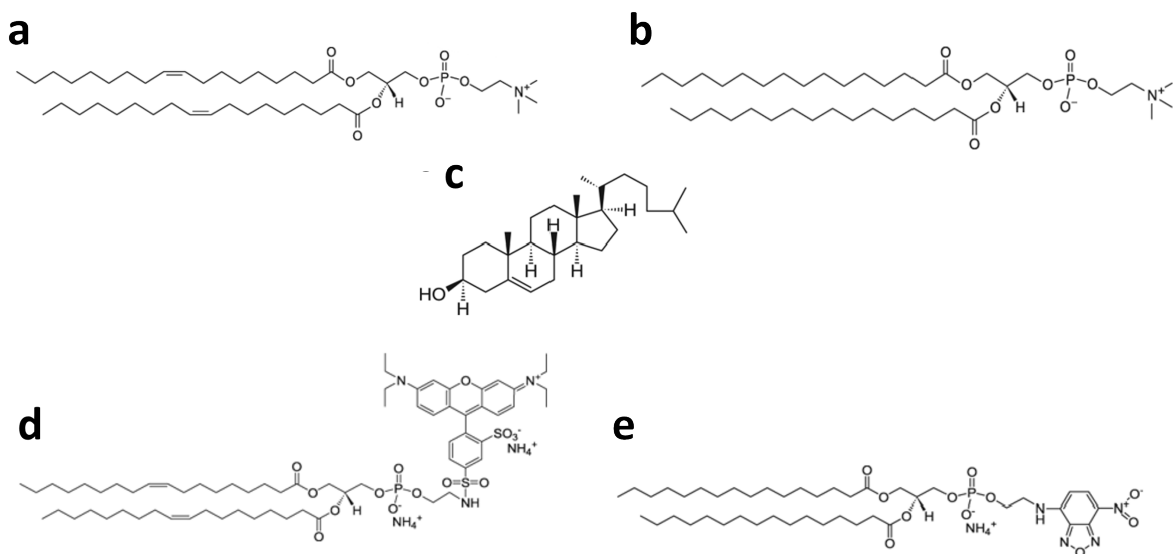


Figure 1: **Chemical structure of the various phospholipids used to fabricate the Janus GUVs a, DOPC, b, DPPC, c, cholesterol, d, RhPE and e, NBDPE.**

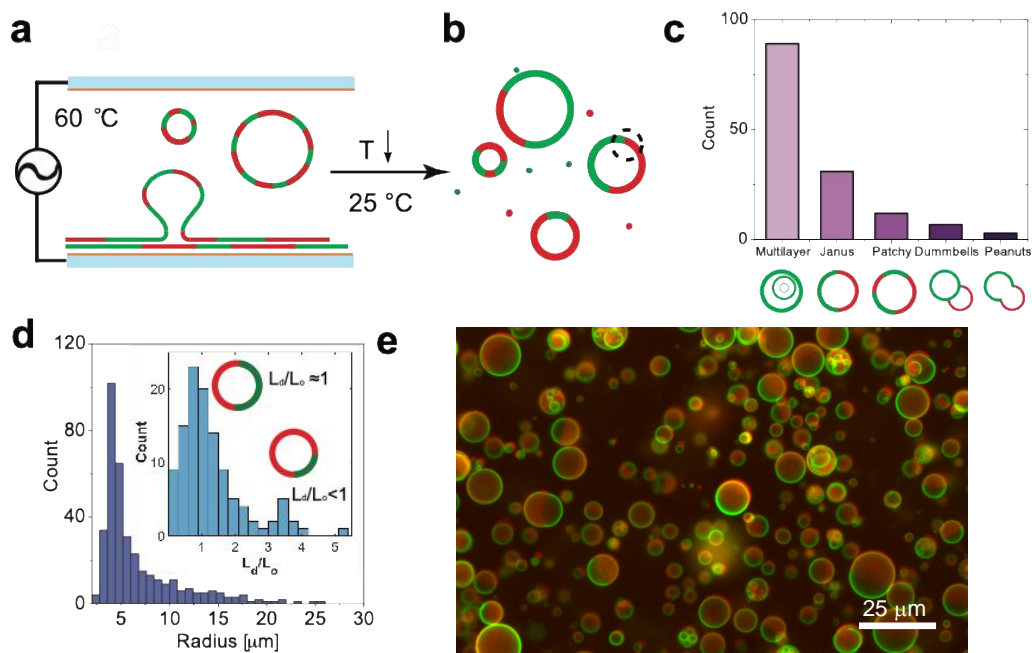


Figure 2: Fabrication and characterization of Janus GUVs **a**, Scheme of the electroformation process where the dried layers of the lipid mixture are hydrated in water and 25 mM Sucrose at 60° C in between two electrodes while applying an AC electric field. **b**, Upon cooling to 25° C, spontaneous phase separation arises leading to liquid-liquid phase-separated GUVs with two lipid domains (red and green). **c**, Population distribution of the various geometries obtained. **d**, Size distribution of the spherical Janus GUVs, and asymmetry (inset) distribution as the ratio of the liquid-disordered (L_d , red) and the liquid-ordered (L_o , green) phases obtained from electroformation. **e**, Fluorescent microscopy picture of a typical sample of Janus GUVs. The scale bar depicts 25 μm .

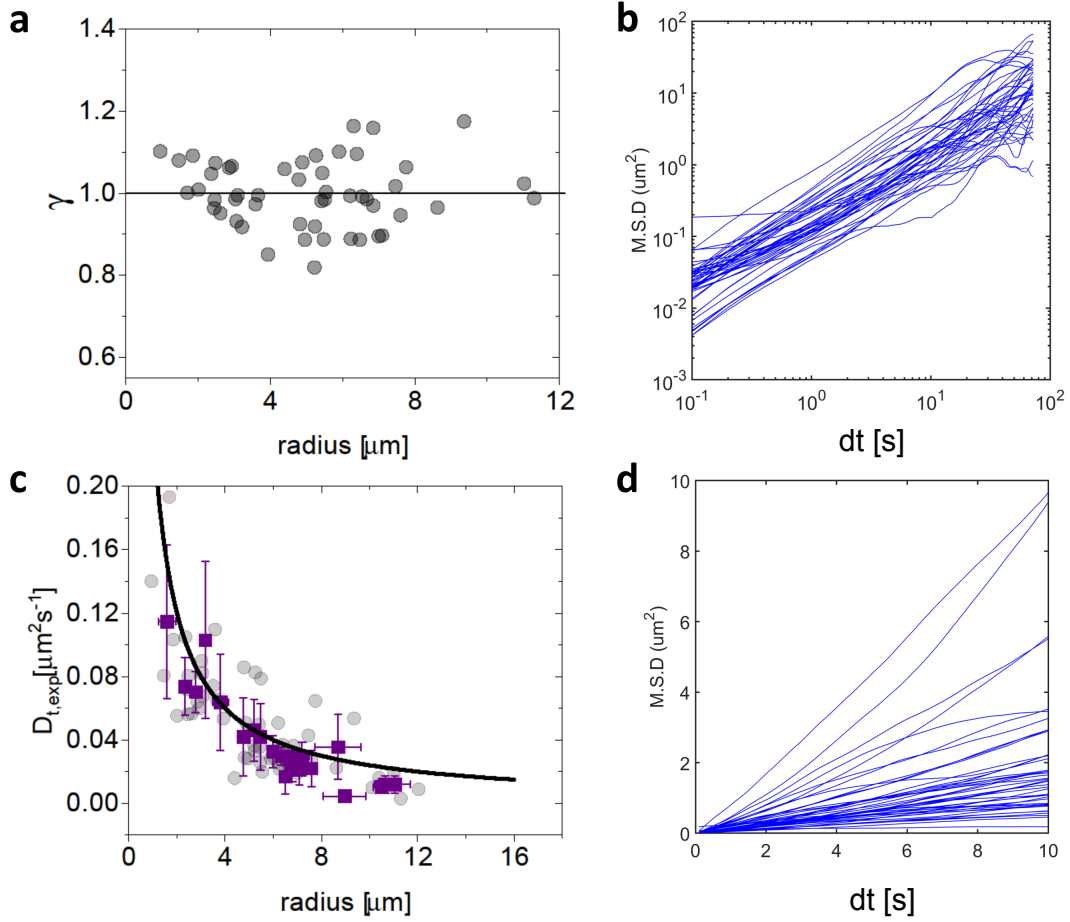


Figure 3: **Passive dynamics of spherical Janus GUVs** **a**, Values of γ as a function of size, obtained by fitting the slope of MSD curves of passive vesicles in a log-log plot. **b**, Log-log plot of MSD curves of passive vesicles (0 kHz, 0 V_{pp}) used to fit the exponent γ . **c**, Experimental (grey points) and theoretical (black line) translational diffusion coefficients D_T as a function of vesicle size. The purple squares represent the average over three points with error bars. The experimental points were obtained by fitting to the MSD curves of passive vesicles, where $\text{MSD}(t) = 4D_T t^\gamma$, being $\gamma \approx 1$ in the diffusive regime, and the theoretical curve was calculated using the Stokes-Einstein relation $D_T = \frac{k_B T}{6\pi\eta r}$. **d**, MSD curves of passive vesicles (0 kHz, 0 V_{pp}), in a linear plot, used to determine the experimental diffusion coefficient D_T .

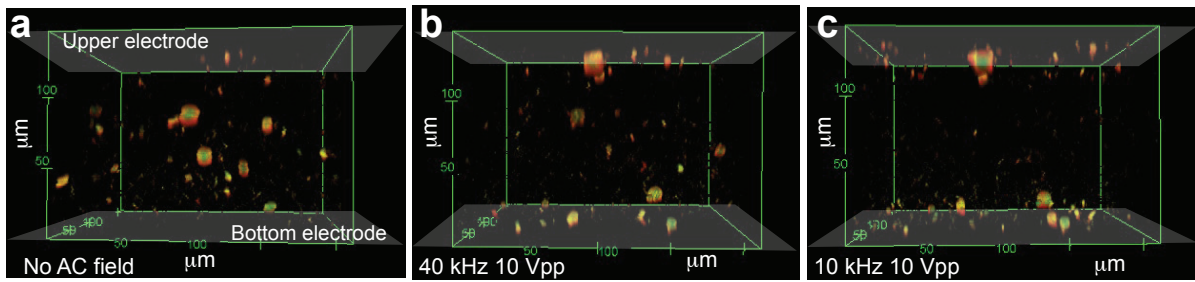


Figure 4: **Behavior of GUVs in parallel electrodes** Confocal images of the phase-separated GUVs, **a**, without AC field, **b**, at 40 kHz and 10 V_{pp}, and **c**, at 10 kHz and 10 V_{pp}. The shaded area indicates the position of the electrode. The x, y and z axes are in μm.

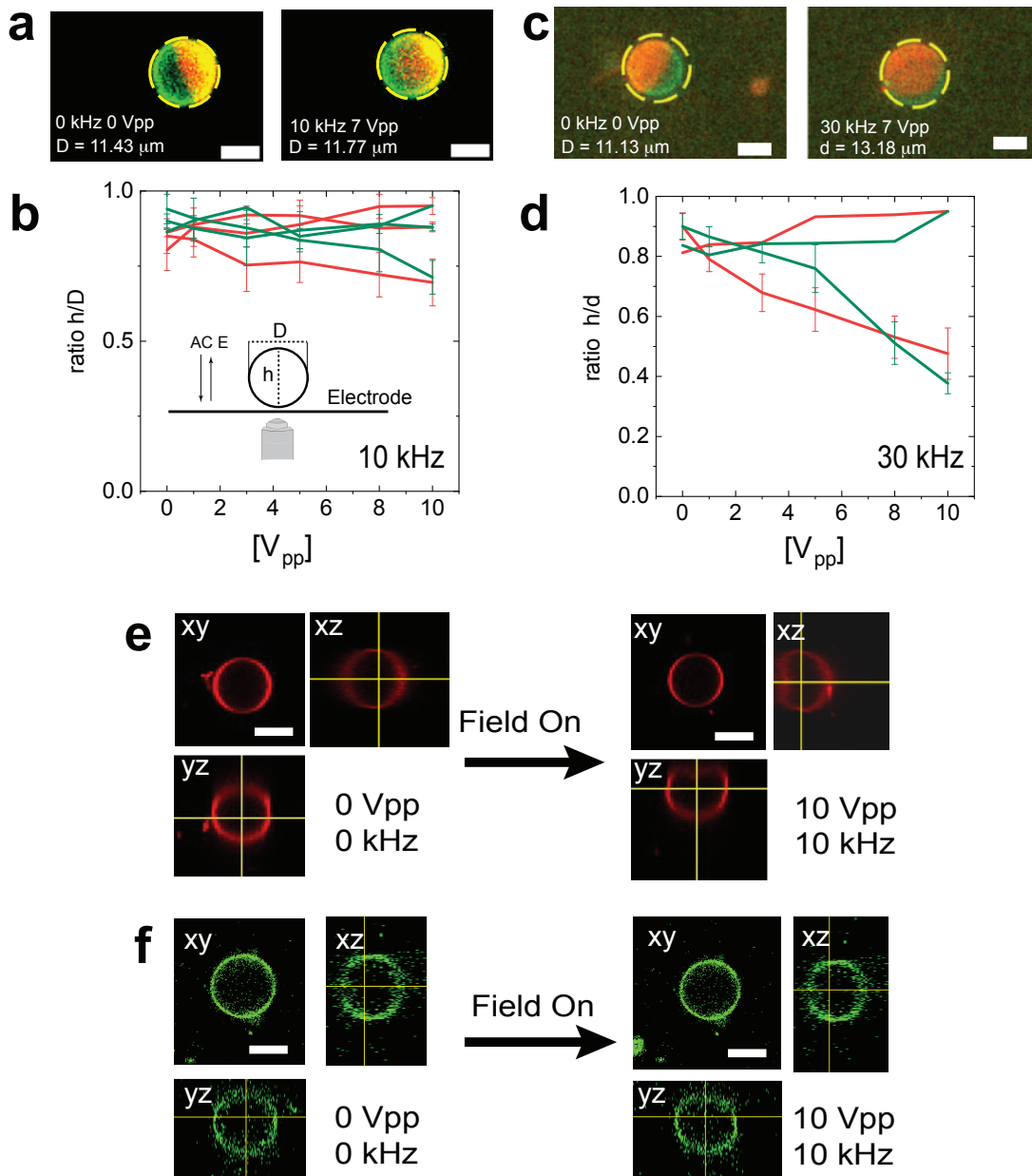


Figure 5: Effect of the AC fields on membrane deformation Fluorescence images taken at the equator of the GUV before and after application of an AC field at **a**, 10 kHz and **c**, 30 kHz and 7 V_{pp} showing the effective deformation of the vesicles. The scale bars depict 5 μm . Confocal microscopy data of the ratio h/D of height h and diameter D of different populations of non-phase separated vesicles as a function of applied voltage at **b**, 10 kHz and **d**, 30 kHz with errorbars showing the standard deviation. Top and side views of **e**, 35:10 DOPC/chol + 0.2% RhPE + 1% NBDPE and **f**, 35:20 DPPC/chol + 1% NBDPE before and after applying an AC field of 10 kHz and 8 V_{pp}. The scale bars depict 10 μm .

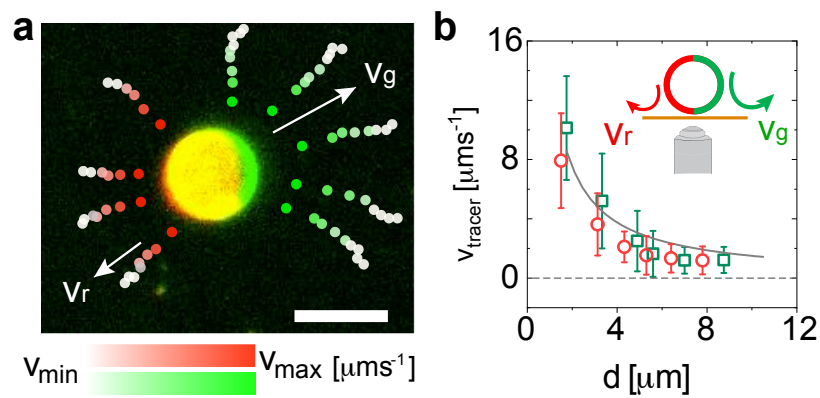


Figure 6: **Electrohydrodynamic flow behaviour on the surface of a membrane** **a**, PIV of tracers trajectories around each hemisphere. The color code gradient indicates the tracer velocity for the L_o (green) and L_d (red) from high to low velocities. The scale bar depicts $10 \mu m$. **b**, Experimental velocity of the tracers v_{tracer} for the L_o (green) and L_d (red) phases as a function of the distance between the GUV and the tracer d . The solid line represents a decay of $\frac{1}{d}$. The error bars are the standard deviation over more than 50 tracers.

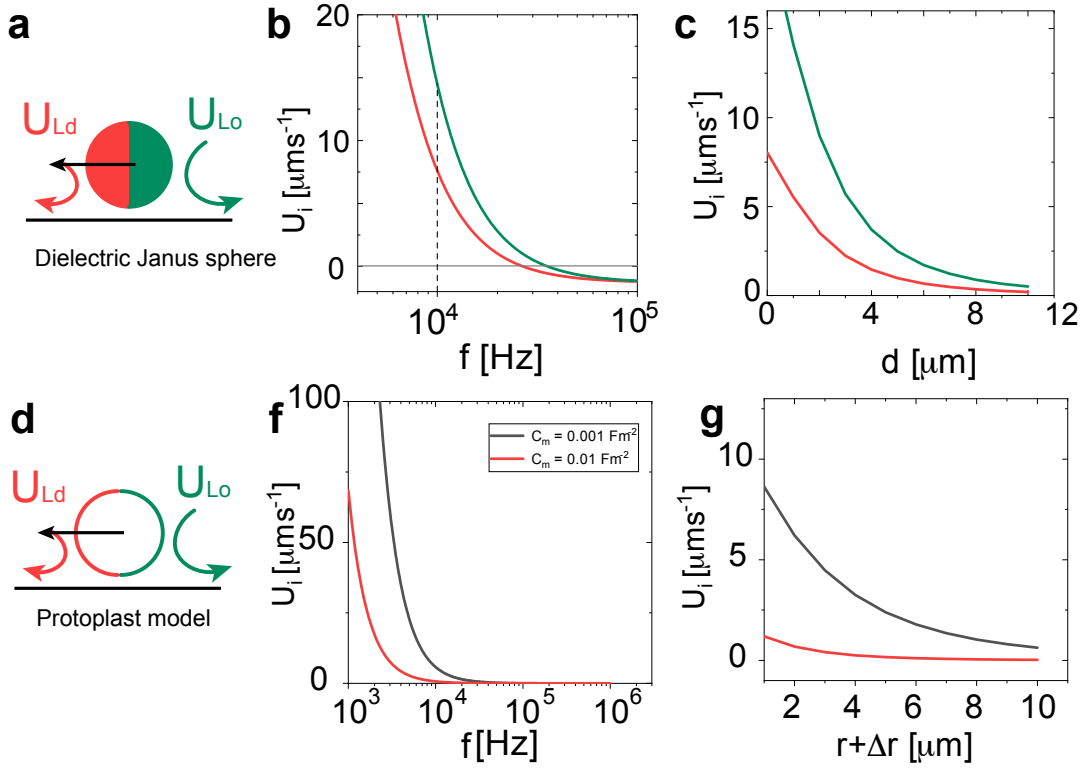


Figure 7: **Theoretical estimation of the EHD flows behavior** Schemes of models used for estimating the EHD flows considering a **a**, hard colloidal particle and **d**, protoplast model (thin shell where the $\sigma_{in} = \sigma_{out}$). The arrows represent the direction and magnitude of each lipid phase. Estimated EHD flows from Eq.S6 using the hard colloidal particle model with the fitting parameters $\beta_1 = 0.2$ (L_o) and $\beta_2 = 0.15$ (L_d) for GUVs of the two GUV lipid phases L_o (U_{L_o}) and L_d (U_{L_d}) as a function of **b**, frequency estimated at $1 \mu\text{m}$ from surface of the GUV, and **c**, at a fixed frequency of 10 kHz as a function of the particle distance. Estimated flow velocity U_i using Eq.S6 and including the complex polarizability K^* using the protoplast model, for membrane capacitance C_m of 0.001 (gray) and 0.01 (red) Fm^{-1} as reference values from typical experimental measurements reported in literature **f**, as a function of the frequency at a distance of the membrane of the GUV and **g**, at fixed frequency and voltage (10 kHz, $9 V_{pp}$) at varying distance from the membrane surface.

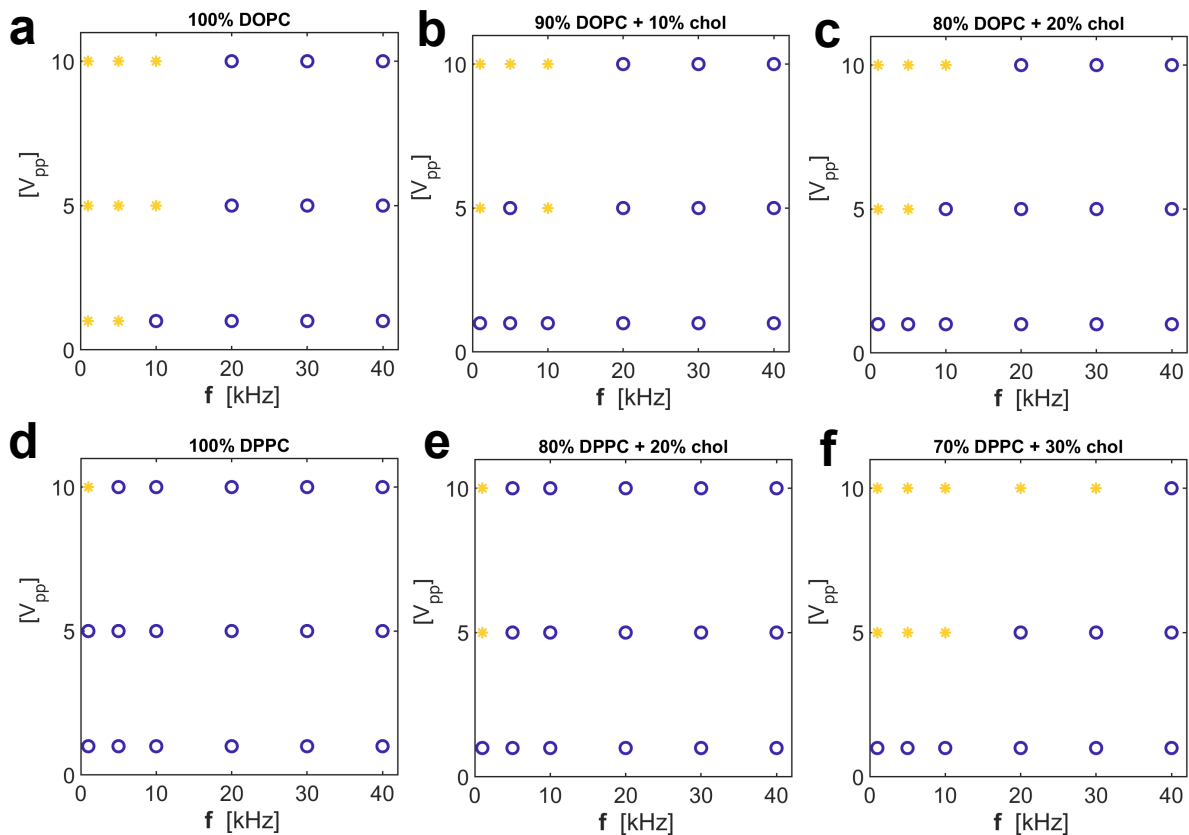


Figure 8: **Dynamical state diagrams of control experiments with non-phase separated vesicles** **a**, 100% DOPC **b**, 90% DOPC + 10% cholesterol **c**, 80% DOPC + 20% cholesterol **d**, 100% DPPC **e**, 80% DPPC + 20% cholesterol **f**, 70 % DPPC + 30 % cholesterol. All DOPC control samples contained 0.1 % RhPE and all DPPC control samples contained 1% NBDPE. Legend: * breaking of vesicles; o no active motion of vesicles

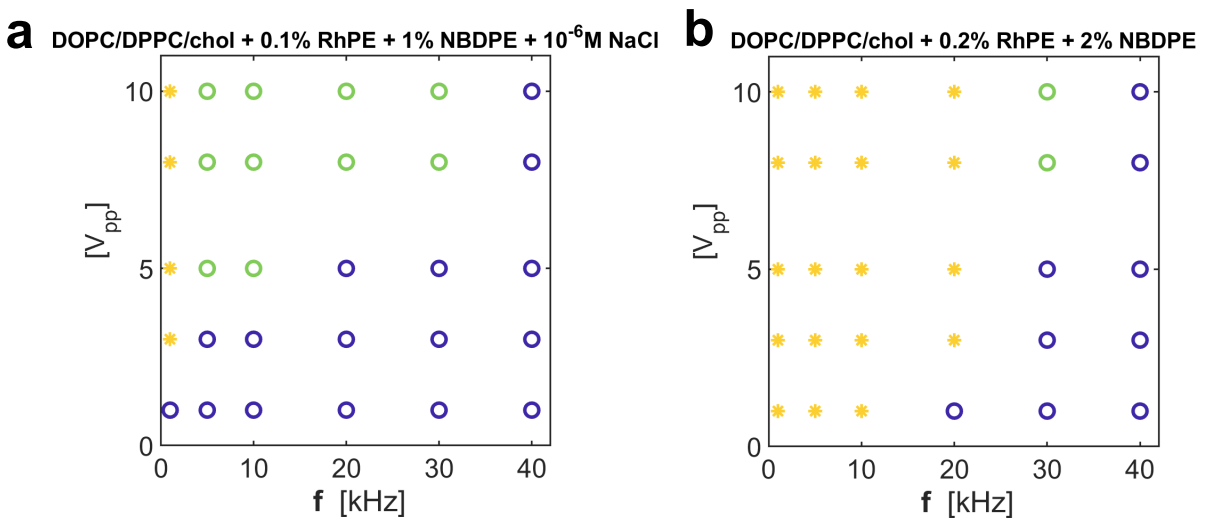


Figure 9: **Dynamical state diagrams of control experiments with phase-separated vesicles**
a, Control experiment with 10^{-6} M NaCl in the surrounding solution. **b**, Control experiment with doubled fluorophore content (0.2% RhPE and 2% NBDPE). Legend: * breaking of vesicles; o active motion of vesicles o no active motion of vesicles

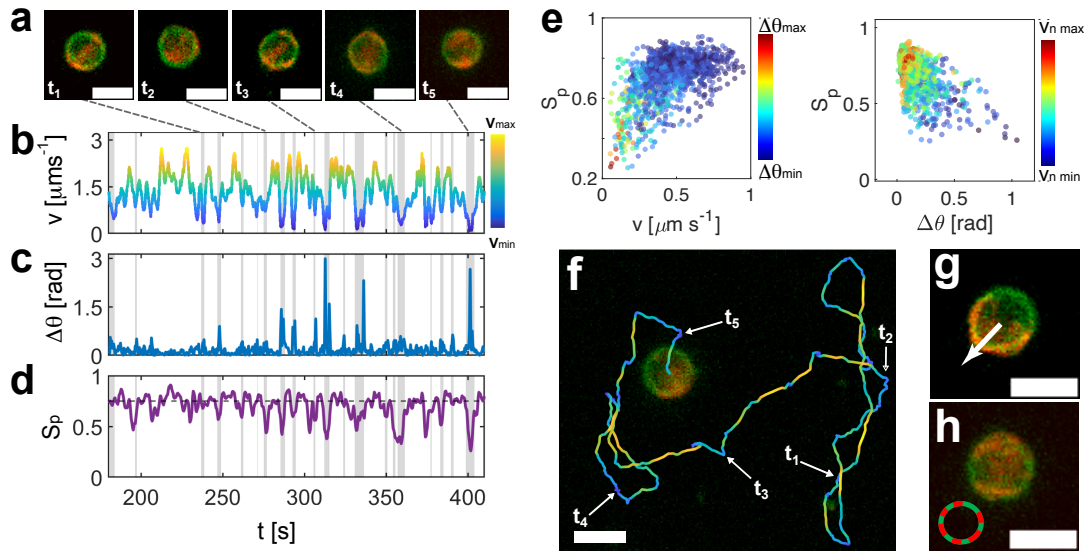


Figure 10: **Analysis of a trajectory depicting run and tumble events at 10 kHz and $9 V_{pp}$** **a**, Snapshots of some identified tumble events. Evolution as a function of time of **b**, instantaneous velocity v , **c**, variation of Janus vesicle orientation $\Delta\theta$ in between two frames, **d**, domain order parameter S_p . **e**, Dependence of the S_p parameter as a function of normalized velocity (left) and $\Delta\theta$ (right). **f**, Fluorescence image using green and red channels overlapping with Janus GUV trajectory, indicating example tumbles from **a**. Examples of domain structure for **g**, run and **h**, tumble events. The scale bar depicts $8 \mu\text{m}$.

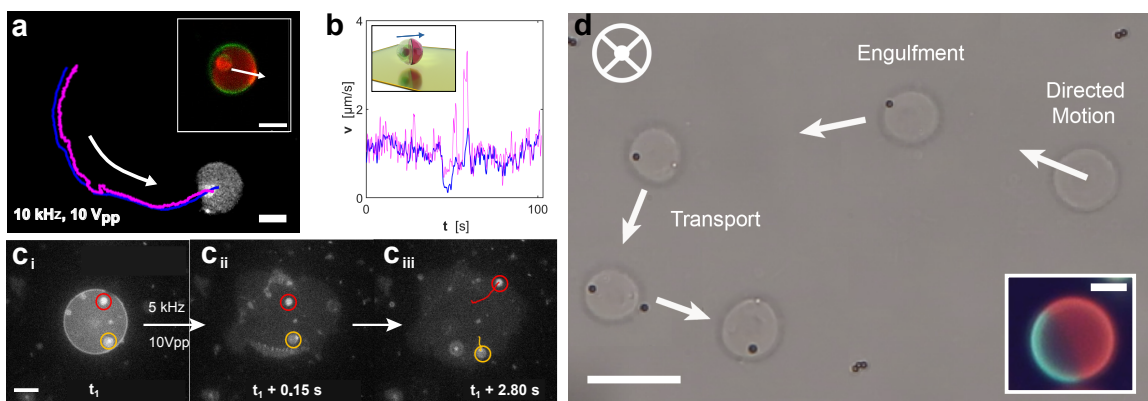


Figure 11: **Uptake, transport and cargo release using active Janus GUVs** **a**, Fluorescence image in BW representing the L_d phase of a GUV, containing a smaller GUV. The pink and blue lines represent the trajectory of the small inner and big outer GUVs, respectively. The inset represents the confocal image of the green and red channels. The scale bar depicts $10 \mu\text{m}$. **b**, Velocity as a function of time for the inner and outer GUVs. The inset represents a schematic representation of the system. **c_i**, **c_{ii}**, **c_{iii}**, Time sequence of on-demand cargo release by bursting the vesicles upon decreasing the frequency to 5 kHz. The scale bar depicts $10 \mu\text{m}$. **d**, Bright field microscopy images of an active Janus vesicle in different stages of swimming, engulfing and transporting a $2 \mu\text{m}$ PS particle at 10 kHz and $9 V_{pp}$. The scale bar depicts $20 \mu\text{m}$. The inset shows the fluorescent image of the same Janus GUV. The scale bar depicts $5 \mu\text{m}$.

Calculation of particles electric properties under AC fields

The time scales (τ_c) of the particle double layer polarization under the effect of an AC electric field have been extensively studied by Squires, Bazant, Ristenpart and Delgado in previous works¹⁻³. These time scales can be extracted from the following expressions,

$$\tau_c = \frac{\kappa^{-1} R}{D_{ions}} \quad (1)$$

where $\sigma_m = 1.5 \times 10^{-5} \text{ Sm}^{-1}$, the Debye length is estimated as $\kappa^{-1} = \sqrt{\frac{\epsilon_m \epsilon_0 D}{\sigma_m}}$, thus $\kappa^{-1} \approx 300 \text{ nm}$ (consistent with solutions in the absence of added ions) as $\epsilon_m = 78$ (MilliQ at 25° C), $\epsilon_0 = 8.854 \times 10^{-12} \text{ Fm}^{-1}$, $D = 2 \times 10^{-9} \text{ m}^2 \text{ s}^{-1}$ considering a general value for ions in the media to be able to do the calculation. With this value of κ^{-1} , we have calculated the new value for the characteristic time for the formation of an induced screening cloud around a particle of radius $R = 5 \mu\text{m}$, where $\tau_c = 700 \mu\text{s}$. In our experiments, we primarily use MilliQ water with low conductivity and 25 mM sucrose ($\sigma_m = 1.5 \times 10^{-5} \text{ Sm}^{-1}$). We also carry out control experiments in 10^{-6} M of NaCl.

For the calculation of the particle conductivity of each phospholipid bilayer phase, we consider a dielectric shell with $\epsilon_p = 10$ on average, in reality having a contrast in dielectric constant between the hydrophobic tail and hydrophilic head⁴. The estimation of σ_p for the phospholipid bilayer surface was assumed to be analogue to a dielectric surface, in which⁵:

$$\sigma_p = \sigma_b + \frac{2K_s}{r} \quad (2)$$

where σ_b is the bulk conductivity (in Sm^{-1}), where for dielectric particles $\sigma_b \approx 0$ ^{6,7}. For the vesicles we considered the bulk conductivity to be the media conductivity $\sigma_m = 1.5 \times 10^{-5} \text{ S m}^{-1}$, as they are filled with 25 mM sucrose solution. This approximation can be used as the charging time of the membrane - acting as a capacitor - $\tau_{c,m}$ is orders of magnitude slower than the applied

frequency $\tau_c \gg \tau_f$, as shown in Table S1 and where τ_f is the inverse of the applied frequency. K_s is the surface conductance (in S) of the particle, and r is the particle radius. The value of K_s can be approximated as

$$K_s = \frac{2\sigma_m}{\kappa} \left[\frac{D^+}{D^+ + D^-} \left(e^{-\frac{z\zeta_p e}{2k_B T}} - 1 \right) (1 + 3m^+) + \frac{D^-}{D^+ + D^-} \left(e^{+\frac{z\zeta_p e}{2k_B T}} - 1 \right) (1 + 3m^-) \right] \quad (3)$$

where σ_m is the medium conductivity, e the electron charge, z the valence of the ions, and ζ_p is the zeta-potential of the particle ($\zeta_{LO} = -45\text{mV}$, and $\zeta_{LD} = -33\text{mV}$). The parameters m^\pm are given as⁸

$$m^\pm = \frac{2\epsilon_m \epsilon_0}{3\eta D^\pm} \left(\frac{k_B T}{ze} \right)^2 \quad (4)$$

which describe the contribution of electro-osmotic ion flux to K_s , where η is the viscosity of the fluid. We, therefore, estimate the magnitude of the surface conductivity of each Janus GUV hemisphere composed of a different lipid type. At this sucrose concentration, the propulsion behavior of the Janus GUVs is the same as in the experiments with only MilliQ water ($\sigma_m \approx 5 \times 10^{-5} \text{ Sm}^{-1}$).

The complex polarizability K^* , or Clausius Mossotti factor for the vesicles was calculated using the expression for a solid colloidal particle (considering the surface conductivity calculated as explained before), as $K^* = (\epsilon_p^* - \epsilon_m^*)/(\epsilon_p^* + 2\epsilon_m^*)$ ⁸ (where ϵ_p^* and ϵ_m^* are the complex permittivities of the particle and the medium, respectively). Moreover, we use the dielectric pro-toplast model with a very thin bilipid layer where the external and internal solutions have the same ϵ and σ , and $[K(\omega)]$ can be simplified as $[K(\omega)] \approx \frac{C_m R - \epsilon_m}{C_m R + 2\epsilon_m}$ ^{9,10}.

Since the membrane acts as a capacitor, we calculate the membrane charging time as¹⁰

$$\tau_{c,m} = RC_m \left(\frac{1}{\sigma_{in}} + \frac{1}{2\sigma_{out}} \right) \quad (5)$$

where R is the radius of the vesicle, C_m the membrane capacitance, and σ_{in} and σ_{out} the inner and outer solution conductivities. We have calculated the charging time scales of our system using the experimental and three different values for C_m covering the reported regimes in literature, to evaluate if charging effects are to be considered at the working frequencies where we observe active motion ($\tau_f = 10 - 30 \mu s$). We used $\sigma_{in} = \sigma_{out} = 1.5 \times 10^{-5} \text{ S m}^{-1}$. The results are shown in Table I below.

Table 1: Calculation of membrane charging times as a function of the membrane capacitance C_m .

C_m [Fm ⁻¹]	$\tau_{c,m}$ [ms]
0.001	0.5
0.01	5
0.1	50

Based on these timescales, and the frequency applied during active motion (10 kHz), the membrane charging effects are negligible in this frequency regime.

Estimation of EHD with colloidal electrokinetic model

The theoretical prediction of the EHDFs generated by a single sphere under an applied AC voltage $V_{pp} e^{-j\omega t}$ has been studied and derived by N. Wu *et al.* in previous works¹¹ (the expression has been corrected from the original article, information shared with the authors via private communication). The EHDFs depend on D (the diffusion coefficient of the ions in the liquid), κ^{-1} (the Debye length) and H (half the separation between the electrodes, $60 \mu m$ in our case). Therefore, the velocity of the EHDF U_i around a single particle of radius R_i at a given reference

distance r_i at which the EHD is evaluated, within 2 electrodes separated by a distance $2H$, can be calculated using

$$U_i = \beta \frac{C}{\eta} \frac{K' + K''\bar{\omega}}{1 + \bar{\omega}^2} \frac{3(r_i/R_i)}{2 [1 + (r_i/R_i)^2]^{5/2}}, \quad C = \epsilon\epsilon_0 H \left(\frac{V_{pp}}{2H} \right)^2 \quad (6)$$

where η is the solvent viscosity and $\bar{\omega} = \omega H/\kappa D$ with frequency ω , κ being the inverse Debye length and D the ion diffusivity in the solvent¹¹. Here, β is a constant prefactor used as a single fitting parameter to obtain the experimental velocities, ϵ is the solvent relative permittivity, ϵ_0 is the vacuum permittivity. K'_i and K''_i are the real and imaginary part of the particle's Clausius-Mossotti factor K_i^* , $K^* = K' + iK''$ ⁵. They play a key role in calculating U_i , as they determine the sign of the EHDF. The Clausius-Mossotti factor is often used to describe the polarizability of a particle suspended in a fluid. It dictates the magnitude and sign of the induced dipole moment, and therefore also the distortion of the fluid flows of charged particles under an AC electric field^{5,12}.

Thus, the magnitude and direction of the EHD flows (U_i) depend mainly on the contrast between the complex polarizability of the particles relative to the surrounding medium as $U_i \propto K'_i + K''_i$. As previously mentioned, the Clausius Mossotti factor depends on the dielectric properties of the particles as $K^* = (\epsilon_p^* - \epsilon_m^*)/(\epsilon_p^* + 2\epsilon_m^*)$ ⁸, where ϵ_p^* and ϵ_m^* are the complex permittivities of the particle and the medium, respectively. ϵ_p^* can be written as $\epsilon_p^* = \epsilon_0(\epsilon'_p - j\sigma'_p/\omega) = \epsilon_0\epsilon'_p - j\sigma'_p\omega^{-1}$, where ϵ'_p and σ'_p are the real parts of the particle permittivity and conductivity, respectively, and $j = \sqrt{-1}$. This system is sensitive to contrast in medium and particle surface conductivities, determining the final EHD flows. Finally, to evaluate the EHD flows around each lipid phase at various distances, we consider an initial r_i as the distance from the centre of GUV and we vary the distance from the particle.

We also tested the protoplast model to calculate K^* (fig.S7), considering a very thin bilipid layer where the external and internal solutions have the same ϵ and σ and $[K(\omega)]$ can be sim-

plified as¹⁰ $[K(\omega)] \approx \frac{C_m R - \epsilon_m}{C_m R + 2\epsilon_m}$, where C_m is the membrane effective capacitance, and R is the radius of the vesicle. This model is sensitive to membrane capacitance, defining the magnitude and direction of the EHD flow. While here we do not have direct access to $C_{m,green}$, based on the calculated results we might argue that $C_{m,green}$ needs to be smaller than $C_{m,red}$ for the magnitude of the EHD flow around the green to be dominant (motion towards the red side).

Detection of run-and-tumble events and analysis

We detect the running and tumbling events that occur in a trajectory using two criteria, namely that tumbles exhibit large decreases in velocity as well as large changes in the orientation angle. This approach was adapted from previous works by Najafi et al¹³ and Seyrich et al¹⁴. We calculate the instantaneous velocity at each step of the trajectories that were previously determined via particle tracking algorithms and then smoothed using the *smooth* function in Matlab to reduce noise. Subsequently, we determine the time t_{min} of the local velocity minima $v(t_{min})$ and the depth of these local minima as

$$\Delta v = v(t_{max}) - v(t_{min}) \quad (7)$$

where t_{max} is the local velocity maximum closest to $v(t_{min})$. If Δv is larger than a threshold value, in this case, 70% of $v(t_{min})$, being $\Delta v \geq 0.7v(t_{min})$, then the minimum is counted as a potential tumble. We determine the width of the minima in order to detect the length of the tumble. For this, we use

$$0.3\Delta v + v(t_{min}) \geq v(t) \quad (8)$$

where the difference in velocities at the minimum t_{min} and the velocity at time t adjacent to the minimum should not be larger than 30% of Δv in order to be part of the tumble. If t is counted as part of the tumble, the next point $t + 1$ is evaluated until equation 8 is not fulfilled

anymore. We choose and tune the threshold values empirically by comparing the results of the run-and-tumble analysis to videos of some of the vesicles.

For the second criterion, we consider the change in orientation angle $\Delta\theta$ at each step of the trajectory. As the difference between the angles does not exhibit the same drops as the velocity does and thus it was not possible to find a universal threshold value without receiving many false positives, we use a different approach to determine potential tumbles. We consider the distribution of $\Delta\theta$ which exhibits a narrow high peak containing the small orientation changes of the runs and large tails which represent the large orientation changes of the tumbles. We separate them into two separate Gaussian distributions using the Matlab function *fitgmdist*. The distribution obtained from the tails contains the local maxima of the change in orientation angles $\Delta\theta(t_{\max})$ and we consider these points of the trajectories as potential tumbles as well. The length of these tumbles is given by

$$0.2|\Delta\theta(t_{\max})| \leq |\Delta\theta(t)| \quad (9)$$

with which the changes of angles $\Delta\theta$ at times t surrounding the local maxima are included in the tumble if they are larger than 20% of $\Delta\theta(t_{\max})$.

Finally, we combine both conditions so the parts of the trajectories to which both conditions apply are detected as tumbles, while the remaining parts of the trajectory are classified as runs.

Order parameter analysis: For the purpose of analysis, the 2D images of the Janus GUVs are "unwrapped" into a 1D signal representation. The unwrapping process involves tracing around the perimeter of the vesicle in the 2D image and converting this trace into a 1D sequence. This sequence, or signal, maintains the order of red and green labels as they appear around the vesicle's circumference. The unwrapping ensures that the spatial relationships between different regions on the vesicle are preserved in the 1D representation. Once the 1D signal is generated,

we precisely identify transitions between regions labelled red and green. These transitions demarcate the boundaries of contiguous segments, allowing us to measure their spatial extent. Such measurements provide quantitative insight into the spatial persistence of each label. Next, we measure the angular distribution by the midpoints of these segments, that are computed and converted to angular coordinates, with the full circumference of the vesicle equated to (2π) . This transformation facilitates quantitative analysis of the relative positioning of labelled segments around the vesicle. By computing angular differences between adjacent midpoints, we determine the degree of spatial uniformity in label distribution.

Gradient Calculation and identification of transitions. Given the 1D signal, S , of length N , the gradient is computed to identify the transition points between the red and green labels:

$$\nabla u_i = u_{i+1} - u_i \quad (10)$$

Considering the periodic boundary conditions:

$$\nabla u_N = u_1 - u_N. \quad (11)$$

The transition from green to red is indicated by a gradient of +1, and from red to green by a gradient of -1. Based on these transitions, we identify the start and end of each step. Next we can compute the length of each step, L , is computed as:

$$L_i = \text{End}_i - \text{Start}_i, \quad (12)$$

where End_i and Start_i represent the end and start of the i^{th} step, respectively. Once we have the Start_i and the length of the step L_i we can compute the angular position of each step by first computing the midpoint of each step, and then the position is converted to an angular value considering the full signal:

$$\theta_i = \left(\frac{\text{Midpoint}_i}{N} \right) \times 2\pi \quad (13)$$

Signal Fragmentation. The gradient of the signal, capturing differences between successive data points, indicates transitions between labelled regions. The sum of the absolute values of this gradient provides a metric for the overall fragmentation of the signal:

$$F = \sum_i |\nabla u_i|, \quad (14)$$

where F denotes the fragmentation measure, and ∇u_i represents the gradient at the i^{th} position. An increase of F suggests increased fragmentation, indicative of frequent transitions between labelled regions. Note that when the system is fully separated, i.e there are only two regions, the value of $F = 2$ and when the system is at the maximum disorder the value of F would be equal to the number of pixels, N , being measured.

Simulation of Active Brownian and Run and Tumble

Here, we use two models to compare the experimental results with numerical simulations.

Active Brownian Particles: We simulate the dynamics of the ABPs by solving the equations of motion in the over-damped limit as¹⁵ :

$$\begin{aligned} x_i &= x_{i-1} + v \cos\varphi_{i-1} \sqrt{2D_T \Delta t} \xi_{x,i} \\ y_i &= y_{i-1} + v \sin\varphi_{i-1} \sqrt{2D_T \Delta t} \xi_{y,i} \\ \varphi_i &= \varphi_{i-1} + \Omega \Delta t + \sqrt{2D_R \Delta t} \xi_{\varphi,i} \end{aligned} \quad (15)$$

where v is the velocity of the particle, Ω the angular velocity, and ξ represent independent white noise processes.

We simulate the motion of ABP of the size of our vesicles, with $R = 3 \pm 2.1 \mu\text{m}$, and average velocity $v = 1.1 \mu\text{ms}^{-1}$ from instantaneous velocities differentiating the run and tumbles. Given the absence of torque a priori on our particles, we set the angular velocity Ω to zero. The temperature is set at 298 K and the viscosity η of MilliQ water with 25 mM of sucrose of 0.001 Pas. The

translational and rotational diffusion coefficients, D_T and D_R , are given by the Stokes-Einstein equations. We run simulations for a total number of 50'000 steps, with a dt of 0.4 s between each step, corresponding with the time resolution of our experiments.

Run and Tumble Particles: We based our simulations on the RTP model to describe the observed run and tumble dynamics of the Janus GUVs, adjusting to the experimental parameters from Seyrich et al.¹⁴. Thus, we simulate the state of a particle by determining each state's durations by generating a random number that is exponentially distributed around the experimental mean run \bar{t}_{run} and mean tumble times \bar{t}_{tum} . If the particle is in a tumbling state, it exhibits no self-propulsion, causing the velocity term to approach zero. Therefore, the particle experiences only reorientation and translational diffusion given by the effective rotational and translational diffusion coefficients $D_{R,\text{eff}}$ and $D_{T,\text{eff}}$ respectively, which are determined from experimental data. We simulate the tumbles by solving the following Langevin equations.

$$\begin{aligned}x_i &= x_{i-1} + \sqrt{2D_{T,\text{eff}}\Delta t}\xi_{x,i} \\y_i &= y_{i-1} + \sqrt{2D_{T,\text{eff}}\Delta t}\xi_{y,i} \\ \varphi_i &= \varphi_{i-1} + \sqrt{2D_{R,\text{eff}}\Delta t}\xi_{\varphi,i}\end{aligned}\tag{16}$$

When the particle switches to the run state we solve the same overdamped Langevin equations as in the ABP model, substituting the velocity v for the velocity of the runs v_{run} .

Mean Square Displacements (MSD)

The MSD of the GUVs was calculated using the x- and y-coordinates of the trajectories of the microswimmers obtained from particle tracking according to equation 17.

$$MSD(t) = \langle (r(t) - r(0))^2 \rangle = \frac{1}{N} \sum_{i=1}^N ((x_i(t) - x_i(0))^2 + (y_i(t) - y_i(0))^2)\tag{17}$$

The MSD of Brownian motion in two dimensions is described by equation 18,

$$MSD(t) = 4D_T t^\gamma \quad (18)$$

where D_T is the translational diffusion coefficient, t is the time and γ is an exponent describing the type of motion the GUV exhibits. To determine this exponent, the slope of the MSD curve in a log-log-plot which corresponds to γ can be determined. For $\gamma \approx 1$ the motion of the vesicle is Brownian and for $\gamma > 1$ the MSD increases exponentially as the Janus GUV experiences propulsion and exhibits active motion. The experimental diffusion coefficient D_T was determined by fitting the MSD curve to equation 18. The theoretical diffusion coefficient $D_{T,Theo}$ can also be calculated using the Stokes-Einstein relation (eq. 19)

$$D_{T,theo} = \frac{k_B T}{6\pi\eta R} \quad (19)$$

where k_B is the Boltzmann constant, T is the Temperature, η is the viscosity of the surrounding medium and R is the radius of the particle.

Active motion is defined as:

$$MSD(t) = 4D_T t + v^2 t^2 \quad (20)$$

where the first term accounts for the Brownian motion and the second term represents the active propulsion. Over short times ($t \ll \tau_R$) this trajectory will be ballistic. Its MSD can be fitted to equation 20, using D_T values obtained from fitting the passive trajectories, to determine the propulsion velocity v .

Over long times ($t \gg \tau_R$) rotational diffusion becomes unnegligible. Therefore, the expression for the MSD will also include diffusive terms (eq. 21) and the MSD curves will show a crossover from ballistic to diffusive motion at the rotational diffusion time τ_R ¹⁶.

$$MSD(t) = 4D_T t + 2v^2 \tau_R^2 \left(\frac{t}{\tau_R} + e^{-\frac{t}{\tau_R}} - 1 \right) \quad (21)$$

The rotational diffusion coefficient $D_R = \tau_R^{-1}$ can also be found by fitting the MSD to equation 21. Similarly to $D_{T,Theo}$, the theoretical $D_{R,Theo}$ can also be calculated using the Stokes-Einstein relation (eq. 22)¹⁷.

$$D_{R,Theo} = \frac{k_B T}{8\pi\eta R^3} \quad (22)$$

List of Supplementary Videos

- **Video S1:** Passive dynamics of Phase-separated passive giant unilamellar vesicles (GUVs). Phase-separated passive giant unilamellar vesicles (GUVs) exhibiting Brownian motion in the absence of an external AC field. RhPE segregates into the liquid-disordered phase (red) and NBDPE is distributed in the whole vesicle (green). Scale bars indicate $20 \mu\text{m}$.
- **Video S2:** Vesicle bursting at low frequencies. Example of a vesicle bursting in real-time upon lowering the frequency of the applied AC field from 10 kHz to 1 kHz at $10 V_{\text{pp}}$. The scale bar indicates $25 \mu\text{m}$.
- **Video S3:** Active motion of Janus GUVs. Examples of phase-separated Janus vesicles with asymmetry and their active motion under AC electric field of 10 kHz and $9 V_{\text{pp}}$. The scale bars are $50 \mu\text{m}$.
- **Video S4:** Flow identification with tracers around the GUVs. Movie showcasing small tracers being pushed by EHD flows away from fixed vesicle with single composition GUV (first video), and on an active phase separated GUV (second video), confirming the motion of the vesicles is caused via EHD flows at 10 kHz and $9 V_{\text{pp}}$ in the first example and 5 kHz and $9 V_{\text{pp}}$ in the second example. The scale bar in the first example represents $20 \mu\text{m}$ and the scale bar in the second example indicates $25 \mu\text{m}$.
- **Video S5:** Run and tumble trajectories of GUVs. Three individual examples of single phase-separated vesicles exhibiting active motion via EHD flows at AC field frequencies at different field conditions, with their trajectory colour-coded with their instantaneous velocity v (in $\mu\text{m/s}$) between two frames, going from dark blue (low v) to yellow (high v), and its velocity vector. The first example is at 5 kHz and $9 V_{\text{pp}}$, the second example is at 10 kHz and $7 V_{\text{pp}}$, and the third example is at 10 kHz and $9 V_{\text{pp}}$. The scale bars in all

three examples indicate $15 \mu\text{m}$

- **Video S6:** Motion of GUV containing small GUV. Large vesicle moving with a smaller vesicle inside, acting as a proof of concept for cargo transport with active vesicles moving at 10 kHz and $9 V_{\text{pp}}$. Only the red channel was used during imaging. The scale bar is $10 \mu\text{m}$.
- **Video S7:** Proof of concept of cargo uptake and transport. Janus GUV interacting with a $2 \mu\text{m}$ polystyrene colloid dispersed in the media taken under bright field microscopy. The activity of the Janus GUV is given by the applied AC field at 10 kHz and $8 V_{\text{pp}}$.

References

- [1] M. Z. Bazant and T. M. Squires, *Physical Review Letters*, 2004, **92**, 066101.
- [2] T. M. Squires and M. Z. Bazant, *Journal of Fluid Mechanics*, 2004, **509**, 217–252.
- [3] W. D. Ristenpart, I. A. Aksay and D. A. Saville, *J. Fluid Mech.*, 2007, **575**, 83–109.
- [4] J. Weaver and K. Schoenbach, *IEEE Transactions on Dielectrics and Electrical Insulation*, 2003, **10**, 715–716.
- [5] R. Pethig, *The Clausius–Mossotti Factor*, John Wiley & Sons, Hoboken, NJ, 2017, pp. 119–144.
- [6] C. T. O’Konski, *The Journal of Physical Chemistry*, 1960, **64**, 605–619.
- [7] I. Ermolina and H. Morgan, *Journal of colloid and interface science*, 2005, **285**, 419–28.
- [8] X. Yang, S. Johnson and N. Wu, *Adv. Intell. Syst.*, 2019, **1**, 1900096.
- [9] R. R. Pethig, *Dielectrophoresis: Theory, methodology and biological applications*, John Wiley & Sons, 2017.
- [10] T. B. Jones, *Electromechanics of Particles*, Cambridge University Press, 1995.
- [11] F. Ma, X. Yang, H. Zhao and N. Wu, *Physical Review Letters*, 2015, **115**, 0653.
- [12] V. Shilov, A. Delgado, F. González-Caballero, J. Horno, J. López-García and C. Grosse, *Journal of Colloid and Interface Science*, 2000, **232**, 141–148.
- [13] J. Najafi, M. R. Shaebani, T. John, F. Altegoer, G. Bange and C. Wagner, *Flagellar number governs bacterial spreading and transport efficiency*, 2018, <https://www.science.org>.

- [14] M. Seyrich, Z. Alirezaeizanjani, C. Beta and H. Stark, *New Journal of Physics*, 2018, **20**, 103033.
- [15] G. Volpe, S. Gigan and G. Volpe, *American Journal of Physics*, 2014, **82**, 659–664.
- [16] M. Bailey, A. Sprenger, F. Grillo, H. Löwen and L. Isa, *ArXiv*, 2022.
- [17] G. Dunderdale, S. Ebbens, P. Fairclough and J. Howse, *Langmuir*, 2012, **28**, 10997–11006.